

Space CoBot: a collaborative aerial robot for indoor microgravity environments

Pedro Roque and Rodrigo Ventura

Institute for Systems and Robotics
Instituto Superior Técnico, Universidade de Lisboa
Av. Rovisco Pais, 1; 1049-001 Lisboa, Portugal
pedro.roque@tecnico.ulisboa.pt
rodrigo.ventura@isr.tecnico.ulisboa.pt

Abstract

This paper presents a first contribution to the design of a small aerial robot for inhabited microgravity environments, such as orbiting space stations. In particular, we target a fleet of robots for collaborative tasks with humans, such as telepresence and cooperative mobile manipulation. We explore a propeller based propulsion system, arranged in such a way that the translational and the rotational components can be decoupled, resulting in an holonomic hexarotor. Since propellers have limited thrust, we employ an optimization approach to select the geometric configuration given a criteria of uniform maximum thrust across all directions in the body reference frame. We also tackle the problem of motion control: due to the decoupling of translational and rotational modes we use separate converging controllers for each one of these modes. In addition, we present preliminary simulation results in a realistic simulator, in closed loop with the proposed controller, thus providing a first validation of the followed methodology.

1 Introduction

Multirotor vehicles have recently gained widespread use in various application areas, such as transportation, surveillance, and even entertainment. These platforms are mechanically simple and typically lightweight, resulting in a low cost of acquisition and maintenance. However, to the best knowledge of the authors, there is no known application of multirotor vehicles in space environments. Discarding the obvious impossibility of maneuvering in the absence of air, we consider here the use of these vehicles in human-compatible pressurised spaces under microgravity, such as inside inhabited space stations.

The idea of aerial vehicles inside space stations is not new. The NASA project SPHERES (Synchronized Position Hold Engage Reorient Experimental Satellites) started in 2000 with the design of a small pressurised air propulsion vehicle [9]. In 2006 three SPHERES units were deployed aboard the International Space Station (ISS) [10]. However, the use of pressurised air makes the mechanical complexity significantly higher than a multirotor based solution. More recently, NASA proposed the Astrobee vehicle, with a simpler propulsion system based on several centrifugal fans and nozzles [1]. The Astrobee also features a 2 DoF arm and docking capability.

The most prominent feature of these spaces is the absence of gravity exerted in bodies, that is, the gravity force canceled by the orbital motion of the air mass (microgravity). We will exploit this feature in the following way. Most multirotor orient their propellers vertically along parallel axes. This maximizes thrust vertically in order to compensate for the gravity force. However, in doing so they need to tilt in order to move sideways. Moreover, most of the energy is spent in compensating for gravity. In its absence, not only there is no need to compensate for gravity, but also the energy consumption is expected to be significantly less. We propose to orient the propeller rotation axes non-parallel among them, in such a way we obtain a fully actuated body. That is, to be able to decouple translational from rotational motion. We expect to increase maneuverability, being a particularly relevant feature inside confined spaces such as the interior of a space station.

Fully actuated multirotor have been proposed in the past, but the literature is scarce. In [5, 15] a dexterous hexarotor has been proposed, where the fully actuation feature is used for dexterous manipulation. However, this vehicle is designed for Earth applications, and thus a tradeoff is necessary between dexterity and gravity compensation. Our design is also based in an hexarotor, but since we consider microgravity, we will design the propeller orientation in order to maximize maneuverability along all directions.

The goal of this paper is to present a design of an hexarotor for microgravity environments. We target a multipurpose vehicle, and provide as working examples (1) telepresence, requiring the vehicle to manoeuvre in such a way the screen and camera is pointer towards the party onboard, and (2) mobile manipulation, requiring force closure in order to compensate the reaction force at the end effector. We also consider operational issues such as docking into a charging station and stacking of multiple units in order to save space.

This paper is structured as follows: the requirements and specifications we considered, including a preliminary mechanical design for the vehicle are explained in Section 2, in Section 3 we derive a parametric dynamical model of the vehicle, which is then used in Section 4 for the optimization of the propellers orientation. Section 5 proposes a convergent controller for this fully actuated vehicle, and a preliminary validation in a realistic simulation

environment is presented in Section 6, while Section 7 wraps up the paper with concluding remarks and a reference for future work.

2 Vehicle design

2.1 Requirements

As starting point for the design of the aerial vehicle we considered the following requirements:

1. Safe operation;
2. Self-contained and simple propulsion system, with holonomic kinematics, that is, capable of motion in an arbitrary direction;
3. Autonomous Guidance, Navigation and Control (GN&C);
4. Small dimensions;
5. Modularity;
6. Stackability and docking.

An holonomic kinematics implies the decoupling between translational and rotational motion. That is, the vehicle should not be required to change attitude to move in a given direction. This requirement, together with the one of small dimensions is particularly relevant inside confined spaces such are those of space stations. We also require the vehicle to have an autonomous GN&C, thus simplifying the deployment in already equipment-dense space environments. Modularity is relevant to not only simplify maintenance, but also to allow the vehicle to be extensible. Stackability and docking targets not only the dock into a charging station, but also the possibility of parking them one on top of the others, thus saving space.

2.2 Specification

Our proposed solution is based on a multirotor vehicle, where the propellers are placed in such a way that full holonomy is attained. That is, fully decoupling the translational from the rotational motion, resulting in a 6 Degrees-of-Freedom (DoF) vehicle. The minimum amount of propellers is thus 6, since each propeller corresponds to a single DoF. We propose electric propulsion, due to its simplicity. Since there is no need to compensate for gravity, we expect the energy consumption to be significantly lower than conventional multirotors on Earth.

On Figure 1 we provide a preliminar render for the proposed solution. It is based on 6 electrically powered propellers, protected inside the hull of the vehicle. On the top of the vehicle one can find the docking port, two wide-angle cameras for telepresence and vision-based navigation, and

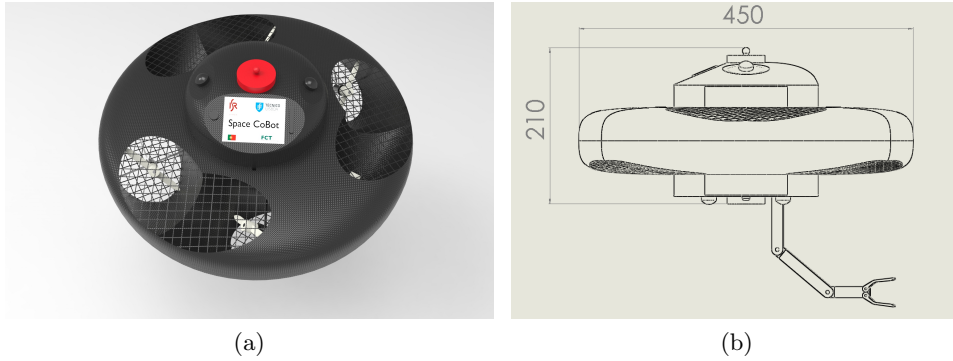


Figure 1: Render of the overall view of Space CoBot (left) and its external dimensions (right).

a screen (with the size of a common smartphone). At the bottom one can find another docking port for stacking, and two more wide-angle cameras. In the following subsections we explain how our design addresses each one of the above mentioned requirements.

The size of the robot in our design is 450mm by 210mm, with a maximum free volume of 2.4 liters for guest modules and experiments. Several images of the Space CoBot are presented below, as well as the overall dimensions in Figure 1(b).

2.2.1 Safety

Safety is a priority on any object, manned or unmanned, aboard a space station. This poses a problem, as most robots are source of acoustic and electromagnetic noise, which shall be kept at a minimum. Along this, we also have the problem of moving objects, such as the propellers, which may cause debris shall any foreign object hit them.

In order to cope with electromagnetic noise, each section of the robot is covered with grounded copper mesh that actuates as a Faraday cage. All motors are protected with a carbon grid to prevent floating objects of reaching the propellers while they are spinning. Proximity sensors are also disposed around the propellers airflow tunnel, to detect and stop the motor in case a small object reaches the propulsion system. To make the vehicle as silent as possible, acoustic absorbing material is placed around the motors cavity.

2.2.2 Propulsion System

Taking advantage of the pressurized atmosphere inside a space station, the proposed propulsion system employs six motors, each with a 4 inches propeller. The selection of electric motors for the propulsion system aims at

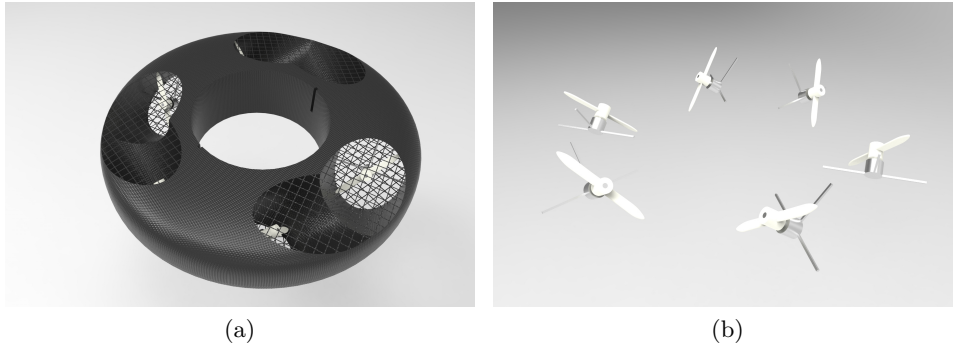


Figure 2: Propulsion system representation: (a) overall view of the module, and (b) relative placement of the propellers.

safety, as it does not have to deal with highly pressurized gas tanks, and can be used with interchangeable batteries or fast-charge docking systems. All the 6 motors are placed along the same plane, 60 degrees away from each other. Each motor is, then, tilted 55 degrees from its vertical axis, providing holonomic motion and enabling total force closure. We defer the justification for this angle to Section 4. All propellers are kept inside the propulsion module and airflow is driven through net protected vents, so to avoid foreign objects of reaching the propeller. The suggested propulsion system is shown in Figure 2.

2.2.3 GN&C System

The navigation and guidance system is based on four wide-angle cameras spread on the top and bottom parts of the device, providing total coverage around the robot. To obtain reliable position and orientation inside the Space Station, robust vision-based algorithms are used in order to locate and navigate the robot. For instance, a combination of stereo and monocular features may be used as proposed in [2].

The control system is composed of a hardware layer and a software stack. The hardware layer is composed by a core system, supporting the base navigation functionalities, and guest systems, allowing for extension modules and scientific payloads. They interface through a distributed communication layer based on parallel protocols. Figure 3 represents the architecture. In green we represent low-level communications and on red high-level ones.

On the software side, a low-level autopilot is responsible for basic pose stabilization and motor driving system, relying on the low-level hardware layer. High-performance algorithms can be deployed on the high-level hardware layer, such as vision-based localization and telepresence audio and video streaming.

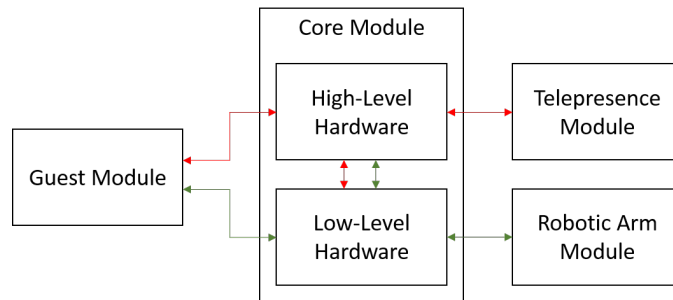


Figure 3: Communications between the various modules of the vehicle.

2.2.4 Modularity

A crucial requirement for maintenance procedures is modularity. For this purpose, we divided the Space CoBot into several detachable modules:

1. *Backbone module*: the backbone module provides support for all modules and constitutes the main component of the Space CoBot. It has slots for all modules, provides data connection through all subsystems and it is capable of delivering power to all components. It provides mounting points for 4 wide-angle cameras for navigation, two on the bottom part of the robot and two on the top side. Also, contains a dome module with a telepresence kit (small computer with a screen, webcam, microphone, and speaker), as well as two wide-angle cameras. Modules are attached through a drawer system, with mechanic and magnetic locking, enabling easy swap-on and preparation for all experiments. Two types of drawers can be used: one with 550 cubic centimeters (standard drawer), and other with 1200 cubic centimeters (double height drawer, approximately).
2. *Propulsion module*: contains all the 6 motors, propellers, and Electronic Speed Controllers (ESC). Connects to the backbone module through low level communication protocols, such as CAN (to provide control on each motor), and two power cables.
3. *Core module*: contains core GN&C systems. It can be fitted into a standard or double height drawer, depending on the computational modules or volume for experiments. A Space CoBot can have simultaneously multiple high-level Core modules (for increased computational power), but only one low-level core module.
4. *Guest modules*: provides the possibility of extending CoBot's functionality with additional modules, such as experimental test-beds for microgravity;

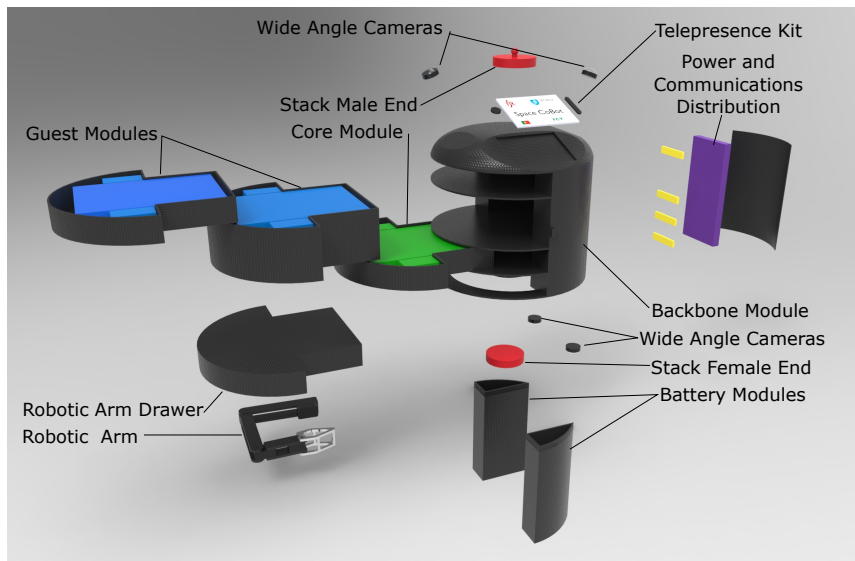


Figure 4: Vehicle modules, excluding propulsion module (see Figure 2).

5. *Robotic arm module*: a robotic arm with 4 DoF is provided, allowing manipulation of objects (such as operational knobs) or grasping dock bars. This module fits in a standard drawer and must be replaced on the bottom slot of the vehicle. If no robotic arm is needed, one may replace the drawer with an additional guest module.

Each module is easily accessible due to the robot layout, and thus it can be easily replaced. A view of all the modules is available on Figure 4.

2.2.5 Stackability

Stackability ensures compact storage of the Space CoBots when charging. All Space CoBots have two stacking components: a male port, at the top, and a female end, at the bottom. These components are placed on opposite sides of the robot, providing physical and electrical coupling. Its cylindrical symmetry simplify docking, as the heading of the robot is not relevant for a successful connection. When stacked, a power connection is made and we are able to charge several Space CoBots at the same time. When one Space CoBot is fully charged, it can detach itself from the stack and the remain robots may re-attach themselves. Figure 5 shows two coupled robots and a detail view of the coupling mechanism. This mechanism is loosely based on the one proposed in [8] for a land robot.

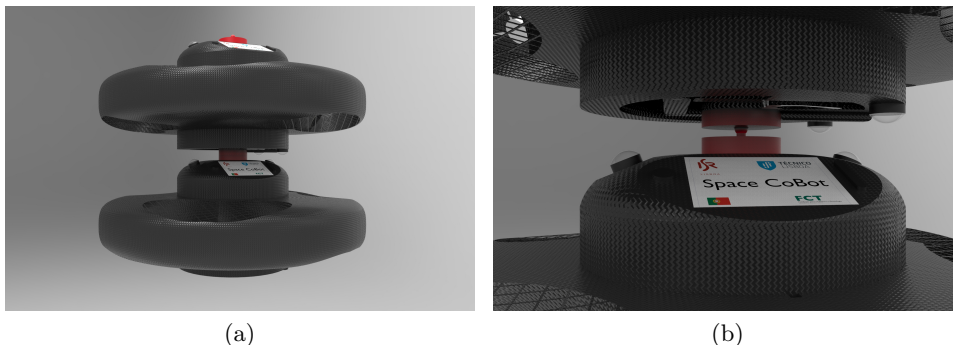


Figure 5: Left: two Space CoBots coupled together; right: coupling mechanism detail.

3 Dynamical model

To derive the dynamical model of the vehicle, we start by modeling the force and torque vectors caused by a single propeller in the body frame denoted \mathcal{B} , whose origin is coincident with the vehicle's center of mass (CoM).

Consider a propeller i whose motor is rigidly linked to the body frame, as depicted in Figure 6. This propeller will generate a force \bar{F}_i and a torque \bar{M}_i with respect to the CoM. While the former results directly from the propeller thrust,

$$\bar{F}_i = f_i \hat{u}_i \quad (1)$$

$$f_i = K_1 u_i \quad (2)$$

where u_i is the actuation signal and f_i is the scalar thrust, the later has two components: the torque caused by the displaced force and the propeller reaction torque:

$$\bar{M}_i = \bar{r}_i \times \bar{F}_i - \tau_i \hat{u}_i \quad (3)$$

$$\tau_i = w_i K_2 u_i \quad (4)$$

where \times denotes vector cross product and w_i is -1 or 1 depending on whether the propeller rotates clockwise or anti-clockwise for a positive forward thrust $f_i > 0$. The constants K_1 and K_2 model a simple linear relationship between the actuation and the scalar thrust force and reaction torque of the propeller. The actuation is often modeled as proportional to the square of the propeller speed of rotation [7].

The relative position of the propeller, \bar{r}_i , orthogonal to the Z axis, and the unit vector \hat{u}_i , aligned with the propeller axis, are uniquely defined by

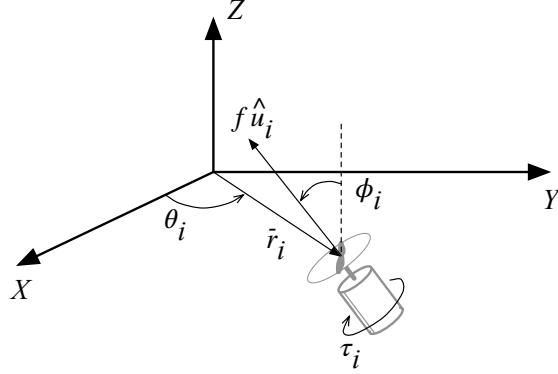


Figure 6: Notation used for modeling a single propeller with respect to the body frame \mathcal{B} , centered on the vehicle's CoM.

the angles θ_i and ϕ_i , and can be easily obtained from geometrical reasoning:

$$\bar{r}_i = \begin{pmatrix} d \cos(\theta_i) \\ d \sin(\theta_i) \\ 0 \end{pmatrix} \quad \hat{u}_i = \begin{pmatrix} \sin(\theta_i) \sin(\phi_i) \\ -\cos(\theta_i) \sin(\phi_i) \\ \cos(\phi_i) \end{pmatrix} \quad (5)$$

where $d = \|\bar{r}_i\|$ is the distance from the propeller to the CoM. Stacking together the resulting force \bar{F}_i and torque \bar{M}_i , one can obtain the linear relation

$$\begin{pmatrix} \bar{F}_i \\ \bar{M}_i \end{pmatrix} = \bar{a}_i u_i \quad (6)$$

where

$$\begin{aligned} \bar{a}_i &= \begin{pmatrix} K_1 \hat{u}_i \\ K_1 \bar{r}_i \times \hat{u}_i - w_i K_2 \hat{u}_i \end{pmatrix} \\ &= \begin{pmatrix} K_1 \sin(\theta_i) \sin(\phi_i) \\ -K_1 \cos(\theta_i) \sin(\phi_i) \\ K_1 \cos(\phi_i) \\ (K_1 d \cos(\phi_i) - w_i K_2 \sin(\phi_i)) \sin(\theta_i) \\ -(K_1 d \cos(\phi_i) - w_i K_2 \sin(\phi_i)) \cos(\theta_i) \\ -K_1 d \sin(\phi_i) - w_i K_2 \cos(\phi_i) \end{pmatrix} \end{aligned} \quad (7)$$

For a vehicle with N propellers, the resulting force and torque will be given by the sum of the contributions of each propeller, given with respect to the CoM, by (6). This sum can be put in matrix form as

$$\begin{pmatrix} \bar{F} \\ \bar{M} \end{pmatrix} = \mathbf{A} \bar{u} \quad (8)$$

where $\mathbf{A} = [\bar{a}_1 \cdots \bar{a}_N]$, hereby called *actuation matrix*, and $\bar{u} = [u_1 \cdots u_N]^T$, the actuation input vector. The crucial observation is that, if the actuation

matrix \mathbf{A} has at least rank 6, the six degrees of freedom of the force and torque combined can be decoupled by solving (8) with respect to the actuation \bar{u} . A necessary (but not sufficient) condition for this to be true is to have at least 6 propellers, as in the hexarotor design considered in this paper. Note that this matrix only depends on the vehicle's design parameters, defined by the angles $\{\theta_i\}$ and $\{\phi_i\}$, distance d , and the trust coefficients K_1 , K_2 , and $\{w_i\}$. However, we will defer the discussion about the properties of this matrix to the next section.

The dynamical model of the vehicle, in the absence of gravity can be derived from the Newton and Euler equations of motion, similarly to [7]. Let us denote the position and velocity of the body frame \mathcal{B} with respect to the inertial frame \mathcal{I} as \bar{x} and \bar{v} , the rotation matrix of frame \mathcal{B} with respect to \mathcal{I} as \mathbf{R} , and the angular velocity of the vehicle in the body frame \mathcal{B} as $\bar{\omega}$. Then,

$$\begin{cases} \dot{\bar{x}} = \bar{v} \\ m\dot{\bar{v}} = \mathbf{R}\bar{F} \\ \dot{\mathbf{R}} = \mathbf{R}\mathbf{S}(\bar{\omega}) \\ \mathbf{J}\dot{\bar{\omega}} = \bar{M} - \bar{\omega} \times \mathbf{J}\bar{\omega} \end{cases} \quad (9)$$

where the constants m and \mathbf{J} are the vehicle's mass and moment of inertia, while $\mathbf{S}(\bar{\omega})$ is the skew-symmetric matrix defined by

$$\mathbf{S}(\bar{\omega}) = \begin{bmatrix} 0 & -\omega_z & \omega_y \\ \omega_z & 0 & -\omega_x \\ -\omega_y & \omega_x & 0 \end{bmatrix} \quad (10)$$

for $\bar{\omega} = [\omega_x \ \omega_y \ \omega_z]^T$.

4 Optimization of the design parameters

In this section we will study how the design parameters translate into the actuation matrix \mathbf{A} defined in the previous section. In particular, we will consider how a bounded actuation translates into maximum values of force and torque. We will then optimize these parameters in order to maximize these values across all directions.

4.1 Problem statement

We will start by considering that each actuation signal is bounded between -1 and 1 , that is,

$$-1 \leq u_i \leq 1 \quad \text{for } i = 1, \dots, 6 \quad (11)$$

According to (8), this hypercube will map onto a 6-dimensional convex polyhedron¹ in the (\bar{F}, \bar{M}) space. Any other choice of bounds is possible by

¹A convex polyhedron is an intersection of a finite number of half-spaces [3].

appropriately scaling constants K_1 and K_2 . However, it assumes that the maximum propeller thrust is symmetric with respect to the direction of rotation. The remaining parameters are the angles $\{\phi_i\}$. We will base our analysis on the optimization of these angles with respect to various criteria.

Our goal will be to find the configurations of angles $\{\phi_i\}$ that maximize the range of forces (and torques) over all directions. Conventional multirotors have all propellers directed at the same direction, *i.e.*, with $\{\phi_i = 0\}$, which maximizes the thrust along that direction. However, they are unable to produce any thrust component over an orthogonal direction. By having nonzero values of $\{\phi_i\}$ we expect to gain thrust over any direction, at the expense of reducing the maximum thrust over some particular one. Geometrically, this corresponds to changing $\{\phi_i\}$ such that a ball of nonzero radius can fit inside the 3-dimensional convex polyhedron in the \bar{F} space mapped by the actuation hypercube in (11), while keeping zero torque, $\bar{M} = 0$. A similar reasoning applies to the torque space \bar{M} , while keeping $\bar{F} = 0$. In sum, we will look for the values of $\{\phi_i\}$ that maximize these radii.

First, we will address the problem of computing the maximum force along a given direction specified as a unit vector \hat{e} , while maintaining a zero torque. From (8), and assuming that \mathbf{A} is full rank, we get

$$\bar{u} = \mathbf{A}^{-1} \begin{pmatrix} \bar{F} \\ \bar{M} \end{pmatrix} = \mathbf{A}^{-1} \begin{pmatrix} F\hat{e} \\ 0 \end{pmatrix} \quad (12)$$

where $F > 0$ is the force magnitude. For what follows, it will be convenient to express the \mathbf{A}^{-1} matrix as blocks of three dimensional row vectors:

$$\mathbf{A}^{-1} = \begin{bmatrix} b_1^T & c_1^T \\ \vdots & \vdots \\ b_6^T & c_6^T \end{bmatrix} \quad (13)$$

where $b_i, c_i \in \mathbb{R}^3$. Then, the actuation of the i -th propeller is given by

$$u_i = F b_i^T \hat{e} \quad (14)$$

Since $|u_i| \leq 1$, we have $F |b_i^T \hat{e}| \leq 1$, and thus F has this upper bound:

$$F \leq \frac{1}{|b_i^T \hat{e}|} \quad (15)$$

Since this inequality has to be satisfied for all propellers $i = 1, \dots, 6$, the maximum force $F_{\hat{e}}^{\max}$ is given by the lowest of these upper bounds

$$F_{\hat{e}}^{\max} = \min_i \frac{1}{|b_i^T \hat{e}|} \quad (16)$$

This force is the maximum force along a given direction \hat{e} . The maximum force attainable in any direction can be obtained by minimising this force

over all possible directions. Since $|b_i^T \hat{e}| \leq \|b_i\|$, this minimum is given by

$$F^{\max} = \min_i \frac{1}{\|b_i\|} \quad (17)$$

The same reasoning can be applied to the torques: consider a torque $\bar{M} = M\hat{e}$ along an arbitrary direction defined by \hat{e} , the corresponding actuation with $\bar{F} = 0$ is $u_i = M c_i^T \hat{e}$, resulting in the following maximum torque along any direction:

$$M^{\max} = \min_i \frac{1}{\|c_i\|} \quad (18)$$

Now, these maximum forces and torque values depend on the design parameters. In the following we will use an optimization approach to find the values of these parameters that maximize the maximum force and/or torque. We will consider the propellers to be equally distributed radially, that is,

$$\theta_i = (i - 1) \frac{\pi}{3} \quad (19)$$

and a fixed distance d , as well as the constants K_1 and K_2 . All the remaining parameters will be the unknown variables:

$$\bar{\psi} = (\phi_1, \dots, \phi_6, w_1, \dots, w_6)^T \quad (20)$$

with the feasibility domain defined by

$$\Psi = \left\{ \bar{\psi} : |\phi_{1,\dots,6}| \leq \frac{\pi}{2}, w_{1,\dots,6} \in \{-1, 1\} \right\} \quad (21)$$

Since we intend to both maximize force and torque, we will model this problem as a multi-criteria optimization problem comprising two cost functions:

$$J_1(\bar{\psi}) = -F^{\max} \quad \text{and} \quad J_2(\bar{\psi}) = -M^{\max} \quad (22)$$

using (17) and (18) computed from the inverse of the \mathbf{A} matrix defined in section 3. This matrix depends nonlinearly on the unknowns $\bar{\psi}$. The solution of this multi-criteria optimization problem is the set P of non-dominated solutions: $\bar{\psi}^0 \in P$ if there is no $\bar{\psi} \in \Psi$ such that $J_i(\bar{\psi}) \leq J_i(\bar{\psi}^0)$ for all $i \in \{1, 2\}$ and $J_M(\bar{\psi}) < J_M(\bar{\psi}^0)$ for at least one $i \in \{1, 2\}$. This set is also called *Pareto optimal set* [13]. A method to approximate this set consists in considering the linear combination of the (22) cost functions, also known as *linear scalarization*:

$$\begin{aligned} J(\bar{\psi}; \lambda) &= (1 - \lambda)J_1(\bar{\psi}) + \lambda J_2(\bar{\psi}) \\ &= -(1 - \lambda)F^{\max} - \lambda M^{\max} \end{aligned} \quad (23)$$

Since these problems cannot be solved in closed form, we will make use of numerical optimization methods. The following section presents the numerical results obtained for this problem.

K_1	K_2	d	$\{\theta_i\}$
5.7	1.3	0.16	in (19)

Table 1: Design parameters of the simulated vehicle.

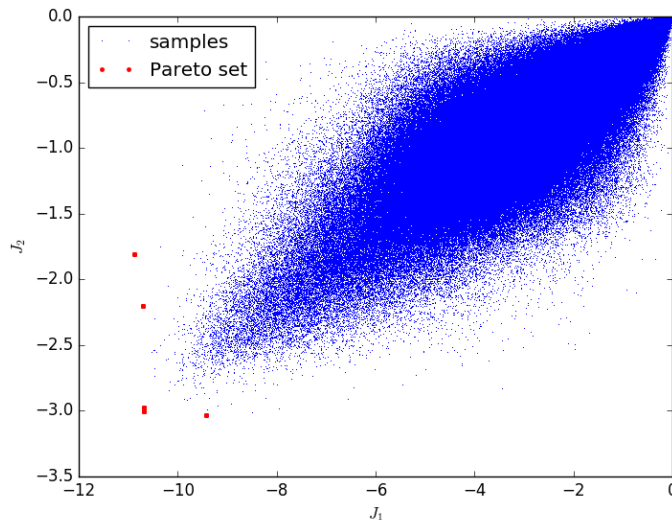


Figure 7: Samples ($N = 10^7$) uniformly drawn from the feasible set Ψ shown in the cost functions space. The non-dominated samples are shown as bigger points.

4.2 Numerical results

We applied this methodology to a vehicle with the design parameters shown in Table 1. The constants K_1 and K_2 have the same values than the ones reported in [4], while d is the one from the design presented in Section 2.2.

To get an idea of the shape of the feasible set in the space of costs values, we sampled N points uniformly from Ψ and identified the non-dominated points. The result is shown in Figure 7. Although these non-dominated points are an unstable approximate to the Pareto optimal set, they suggest that a linear scalarization of the cost functions should provide a good approximation to the actual Pareto optimal set.

The shadow minimum is defined by the optimization of the individual cost functions, that is,

$$J_1^* = \min_{\bar{\psi}} J_1(\bar{\psi}) \quad J_2^* = \min_{\bar{\psi}} J_2(\bar{\psi}) \quad (24)$$

After running differential evolution over 100 runs, we obtained the minimum values $J_1^* = -11.40$ and $J_2^* = -3.176$ (with a total variation below 10^{-3}).

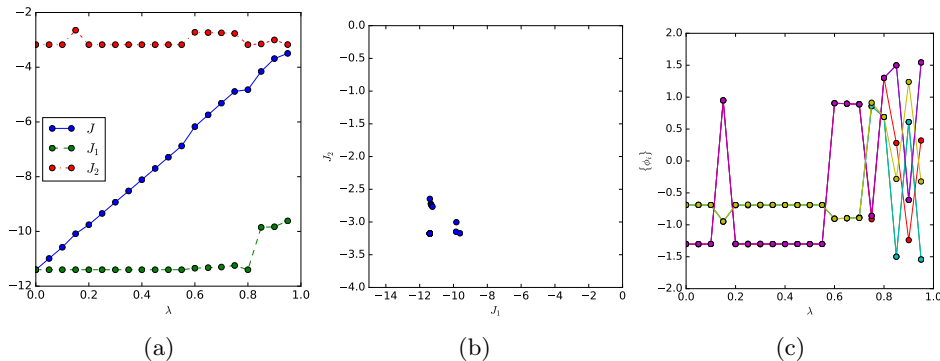


Figure 8: Optimization results, from left to right: (a) plot of J , $J_1 = -F^{\max}$, and $J_2 = M^{\max}$ in function of λ , (b) solutions found shown in the J_1 and J_2 space, and (c) optimized $\{\phi_i\}$ in function of λ .

propeller (i)	1	2	3	4	5	6
θ_i	0°	60°	120°	180°	240°	300°
ϕ_i	-74.54°	-39.54°	-74.57°	-39.48°	-74.49°	-39.46°
w_i	-1	1	-1	1	-1	1

Table 2: The solution found over 100 runs of the optimizer with $\lambda = 0.4$.

We applied the linear scalarization (23) and used a differential evolution² algorithm [14] on this cost function, while ranging λ over an equally spaced grid from 0 to 1 totalling 20 runs. Figure 8 shows the obtained results. The bottom left solution in the 8(b) plot, which approximately dominates all of the others, includes 12 of these 20 runs.

We then ran differential evolution 100 times with $\lambda = 0.4$, an heuristically chosen within a range of λ values where the resulting costs seem stable. From these runs, the dominant solution, found in 24 of these 100 runs, is shown in Table 2. Its costs are $J_1 = -11.40$ and $J_2 = -3.176$, which coincide with the individual minima J_1^* and J_2^* found above. That is, no other solution found has lower cost in either of the cost functions.

To wrap up these results, Figure 9 shows the solutions found by differential evolution as boxplots, in three different scenarios: the solutions for the two shadow minima $\bar{\psi}_1^* = \arg \min J_1(\bar{\psi})$ and $\bar{\psi}_2^* = \arg \min J_2(\bar{\psi})$, and the solutions $\bar{\psi}_\lambda^* = \arg \min J(\bar{\psi}; \lambda)$ for $\lambda = 0.4$. Note that the minimum costs of the $\bar{\psi}_\lambda^*$ solutions coincide with the individual minima of $J_1^* = J_1(\bar{\psi}_1^*)$ and $J_2^* = J_2(\bar{\psi}_2^*)$.

The solution in Table 2 implies three of the propellers to be almost hor-

²We used the implementation found in the *optimize* package of SciPy. We used the default parameters except for a population size of 512 and a mutation dithering range of [0.2; 0.6].

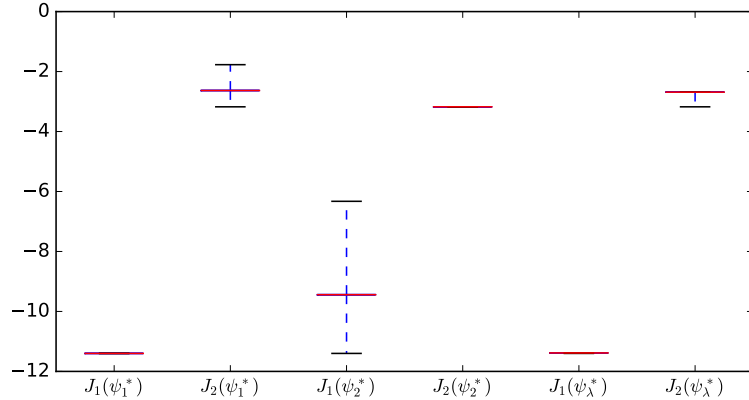


Figure 9: Boxplots of the J_1 and J_2 costs found while separately minimizing, $J_1(\bar{\psi})$ (first and second boxplot), $J_2(\bar{\psi})$ (third and fourth boxplot), and $J(\bar{\psi}; \lambda)$ for $\lambda = 0.4$ (fifth and sixth). Each boxplots represents the minimum, maximum, and median values.

propeller (i)	1	2	3	4	5	6
θ_i	0°	60°	120°	180°	240°	300°
ϕ_i	-55°	55°	-55°	55°	-55°	55°
w_i	-1	-1	1	1	1	-1

Table 3: Design parameters of the selected solution.

horizontal, hindering the air flow to produce the desired thrust. Therefore, we decided on a different solution, with the angle values rounded from an handpicked solution from the Pareto optimal set obtained above. Its parameters are shown in Table 3 and its costs are $J_1 = -F^{\max} = -11.40$ and $J_2 = -M^{\max} = -2.623$, that is, the same maximum force but with 82% of the maximum torque. We preferred this solution because the propeller angles are not as horizontal, resulting in a significantly better air flow.

5 Position and attitude control

The approach used for the motion control of the vehicle exploits its holonomic design by decoupling the translational and rotational modes. To do so, we first apply feedback linearisation [12] to the translational part of (9):

$$\begin{cases} \dot{\bar{x}} = \bar{v} \\ \dot{\bar{v}} = \bar{p} \\ \bar{F} = m\mathbf{R}^T\bar{p} \end{cases} \quad (25)$$

and then design a feedback controller for \bar{p} . Since this dynamical system is second order, a PD controller is enough to ensure convergence:

$$\begin{aligned}\bar{p} &= -k_x \bar{e}_x - k_v \bar{e}_v \\ \bar{e}_x &= \bar{x} - \bar{x}_d \\ \bar{e}_v &= \bar{v} - \bar{v}_d\end{aligned}\tag{26}$$

where \bar{x}_d and \bar{v}_d are the desired position and velocity vectors in the inertial frame \mathcal{I} , and k_x and k_v are the proportional and derivative gains of the PD controller.

For the attitude control we follow the convergent $SO(3)$ controller proposed in [6] for the attitude of a quadrotor, neglecting the Coriolis and the angular velocity reference in the expression for the torque, as suggested in [7]:

$$\begin{aligned}\bar{M} &= -k_R \bar{e}_R - k_\omega \bar{e}_\omega \\ \bar{e}_R &= \frac{1}{2} S^{-1}(\mathbf{R}_d^T \mathbf{R} - \mathbf{R}^T \mathbf{R}_d) \\ \bar{e}_\omega &= \omega - \mathbf{R}^T \mathbf{R}_d \omega_d\end{aligned}\tag{27}$$

where \mathbf{R}_d is the rotation matrix of the desired attitude, ω_d is the desired angular velocity vector, with k_R and k_ω as controller gains. The S^{-1} function performs the inverse operation as the one defined in (10), that is, recovers the vector from a given skew-symmetric matrix.

6 Preliminary validation in simulation

In order to provide preliminar validation of the proposed design, we simulated a simplified model of our robot with V-REP simulation framework [11]. Here, we kept the size of vehicle: all motors are displaced on a 160mm radius circle, 60 degrees apart from each other, and tilted 55 degrees away from their vertical axis (see Table 3), but with different mass and inertia, as we do not know yet have a detail design of the mass distribution. In V-REP we simulated the force and torque produced by each propeller as modeled in (1) and (3). Thus, this simulation aims at the validation of both the design discussed in Section 4 and the controller proposed in Section 5.

This validation was divided into two steps: on the first, each motion mode (translation and attitude) is simulated, first, the position controller, having it move 1 meter on each direction, and then the attitude controller, by moving 70 degrees on each of its axis; on the second, we simulated a path defined by a sequence of waypoints with attitude setpoints, thus combining both controllers.

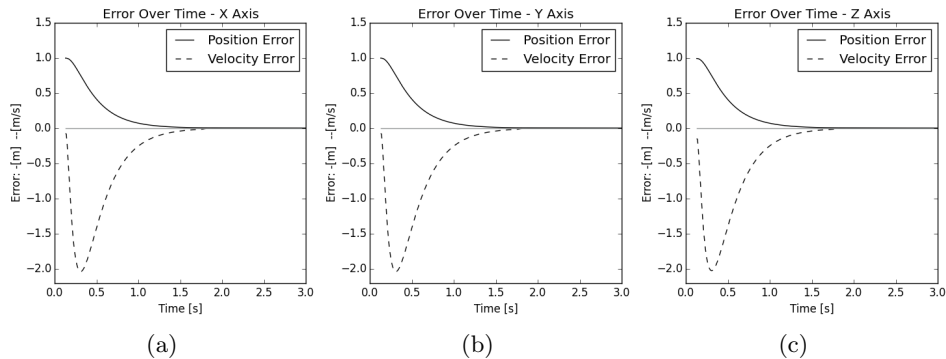


Figure 10: Position Controller Error Convergence: (a) plot of error on X component, (b) plot of error on Y component, and (c) plot of error on Z component.

6.1 Individual motion mode

For this validation, the robot is holding on position $\mathbf{P}_h = (0, 0, 1)$, while the reference is set at $\mathbf{P}_r = (1, 1, 2)$. The total movement of the robot is 1 meter on each direction. On Figure 10 we provide the obtained results for position convergence with the proposed controller in (25) and (26).

The three error plots are approximately equal due to the chosen gains, which are equal on all axis for this experiment: the force applied on each component is only dependent on the mass of the vehicle and position error, and not on the moment of inertia.

For the attitude controller different gains are set according to the moment of inertia of the vehicle, which resulted in a faster response for the X axis then for the Z or Y axis. The attitude of the vehicle starts as $\mathbf{R}_h = (0, 0, 0)$ and the reference is set as $\mathbf{R}_r = (70^\circ, 0, 0), (0, 70^\circ, 0), (0, 0, 70^\circ)$, for rotations along X, Y and Z, respectively. The results are shown in Figure 11.

6.2 Waypoint navigation

To validate the joint position and attitude control, we used waypoint navigation: we created a virtual path composed by 6 setpoints, varying on both position and attitude. The trajectory followed by the vehicle is represented on 12. Plotted are both the X and Y axes of the body frame \mathcal{B} to represent its attitude. We retrieved the errors across the whole trajectory following, for both position and velocity, as well as attitude and angular velocity. These are shown in Figure 13. A video showing this simulation is available online here: <https://youtu.be/BW1Q31ryb9c>

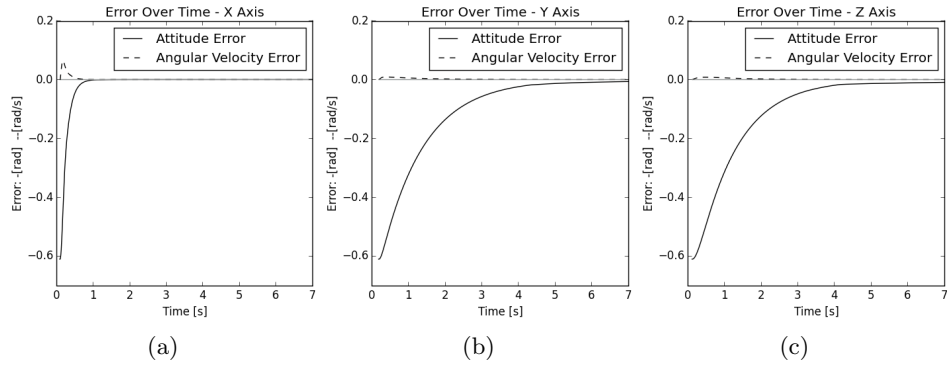


Figure 11: Attitude Controller Error Convergence: (a) plot of error on X component, (b) plot of error on Y component, and (c) plot of error on Z component.

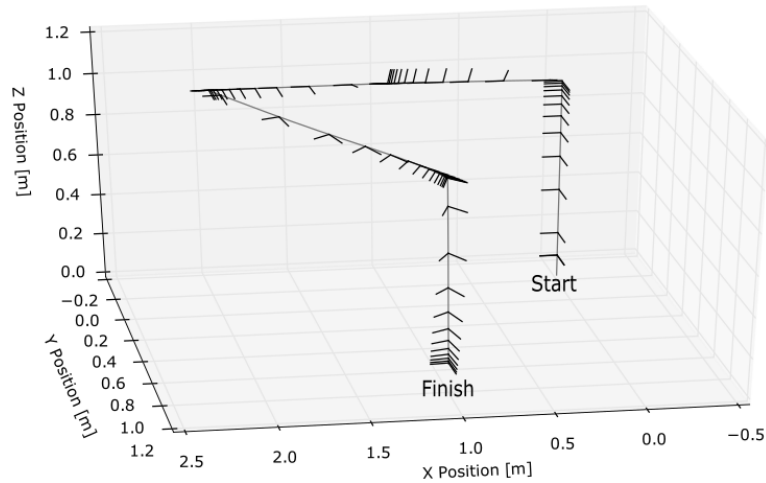
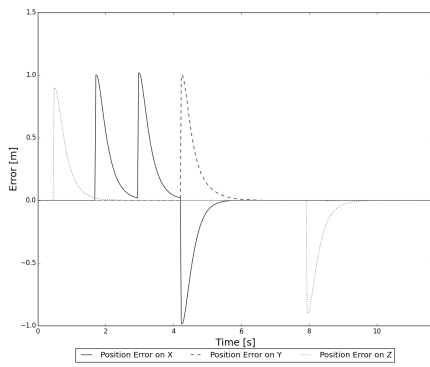
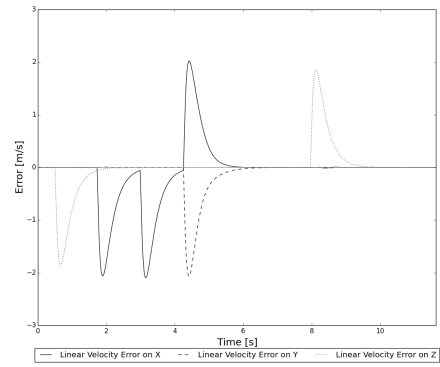


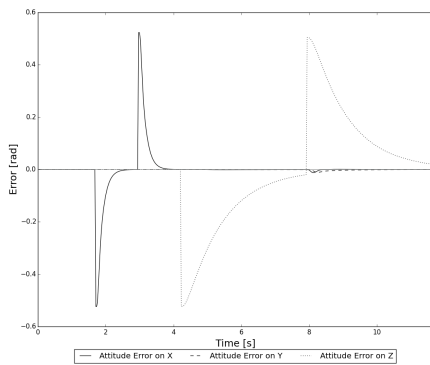
Figure 12: Trajectory followed by the robot. Plotted are X and Y axis of the inertia frame \mathcal{I} .



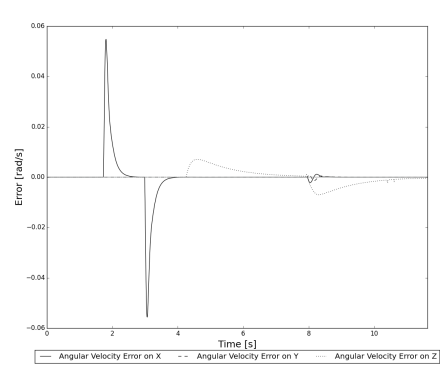
(a)



(b)



(c)



(d)

Figure 13: Waypoint navigation position and attitude errors: (a) error on position, (b) error on linear velocity, (a) error on rotation, and (b) error on angular velocity.

7 Conclusions and future work

This paper presented a concept design of a microgravity holonomic hexarotor. We contribute with a design targeting space stations environments, aiming at collaborative work between the a fleet of these robots and humans. In addition, the solution provides room for extension modules that may be used for increased functionalities and to host microgravity experimental test-beds.

We used an multi-criteria optimization approach to guide the design parameters of the proposed propulsion system. We also proposed a convergent controller for the vehicle, and validated our design in a realistic physics-based simulator. Simulation results show the vehicle navigating between waypoints.

In the future, some work should be done to enhance the design , namely: to study the robustness to the variation of the design parameters around the proposed design, to analyse the controller's robustness to structural and sensor perturbations, and lastly, to validate on the simulator the vehicle with the expected mass and moment of inertia.

Acknowledgments

The authors are grateful to André Santos for the CAD modeling of the vehicle and the renderings presented in this paper. This work was supported by the FCT project [UID/EEA/50009/2013].

References

- [1] Maria Bualat, Jonathan Barlow, Terrence Fong, Christopher Provencher, Trey Smith, and Allison Zuniga. Astrobee: Developing a free-flying robot for the international space station. In *AIAA SPACE 2015 Conference and Exposition*, 2015.
- [2] Filipe Jesus and Rodrigo Ventura. Combining monocular and stereo vision in 6D-SLAM for the localization of a tracked wheel robot. In *IEEE International Symposium on Safety Security and Rescue Robotics (SSRR'12)*, College Station, TX, 2012.
- [3] Melvyn Jeter. *Mathematical programming: an introduction to optimization*, volume 102. CRC Press, 1986.
- [4] Guangying Jiang. Dexterous hexrotor uav platform. Master's thesis, University of Denver, 2013. Paper 321.
- [5] Guangying Jiang and Richard Voyles. Hexrotor UAV platform enabling dextrous interaction with structures – flight test. In *IEEE International*

- Symposium on Safety, Security, and Rescue Robotics (SSRR)*, pages 1–6, 2013.
- [6] Taeyoung Lee, Melvin Leoky, and N Harris McClamroch. Geometric tracking control of a quadrotor UAV on SE(3). In *IEEE Conference on Decision and Control (CDC)*, pages 5420–5425, 2010.
 - [7] Robert Mahony, Vijay Kumar, and Peter Corke. Multirotor aerial vehicles: Modeling, estimation, and control of quadrotor. *IEEE Robotics & Automation Magazine*, (19):20–32, 2012.
 - [8] Carlos Marques, João Cristovão, Paulo Alvito, Pedro Lima, João Frazão, Maria Isabel Ribeiro, and Rodrigo Ventura. A search and rescue robot with tele-operated tether docking system. *Industrial Robot*, 34(4):332–338, 2007.
 - [9] D. Miller, A. Saenz-Otero, J. Wertz, A. Chen, G. Berkowski, C. Brodel, S. Carlson, D. Carpenter, S. Chen, S. Cheng, D. Feller, S. Jackson, B. Pitts, F. Perez, J. Szuminski, and S. Sell. SPHERES: a testbed for long duration satellite formation flying in micro-gravity conditions. In *Proceedings of the AAS/AIAA Space Flight Mechanics Meeting*, 2000.
 - [10] Simon Nolet, Alvar Saenz-Otero, David W Miller, and Amer Fejzic. SPHERES operations aboard the iss: Maturation of gn&c algorithms in microgravity. In *30th Annual AAS Guidance and Control Conference*, pages 7–42, 2007.
 - [11] E. Rohmer, S. P. N. Singh, and M. Freese. V-REP: a versatile and scalable robot simulation framework. In *International Conference on Intelligent Robots and Systems (IROS)*, 2013.
 - [12] Shankar Sastry. *Nonlinear Systems: Analysis, Stability, and Control*. Springer, 1999.
 - [13] Roman Statnikov and J. B. Matusov. *Multicriteria Optimization and Engineering*. Chapman & Hall, 1995.
 - [14] Rainer Storn and Kenneth Price. Differential evolution – a simple and efficient heuristic for global optimization over continuous spaces. *Journal of global optimization*, 11(4):341–359, 1997.
 - [15] Richard Voyles and Guangying Jiang. Hexrotor UAV platform enabling dextrous interaction with structures – preliminary work. In *IEEE International Symposium on Safety, Security, and Rescue Robotics (SSRR)*, pages 1–7, 2012.